A Computational-Experimental Study of Plasma Processing of Carbides at High Temperatures

Final Technical Report

Reporting Period
Start Date: 07/01/2012
End Date: 06/30/2015

Principal Investigator and Co-Investigator
Arturo Bronson and Vinod Kumar

Submitted February, 2016

DOE Research Project: DE-FE0008400
DUNS Number: 13-205-1285

Department of Mechanical Engineering
The University of Texas at El Paso
500 West University, El Paso, Texas 79968-0521

Disclaimer

ABSTRACT

A Computational-Experimental Study of Plasma Processing of Carbides at High Temperatures

Arturo Bronson and Vinod Kumar, The University of Texas at El Paso

The effects of plasma on carbides were computationally investigated for the ultimate development of adherent, dense scales such as Al_2O_3-TiO_2 systems toward oxidation resistance at 1873 K. An alumina scale forms on the carbide because of the significant stability of Al_2O_3 as the outer scale adjacent to the gas phase compared to rutile, though TiO and Ti_2O_3 may form as components of an inner layer of a complicated scale. A sequence of surface reactions starting with the adsorption of oxygen on the surface was applied to experimental data from Donnelly's research group who reported the adsorption of O_2 in a plasma atmosphere as a function of power. In addition to the adsorbed oxygen (O_{ad}) as the rate determining step, it controlled the cascading reaction sequence of the adsorbed species of AlO, AlO_2 and AlO_3, as indicated in the present study. The rate of oxygen adsorption also depends on the ratio of the final to initial adsorbed oxygen as a function the oxygen potential.

In a secondary research thrust, Ti_3AlC was synthesized and subsequently oxidized. A 39Ti-14Al-47TiC (in wt%) mixture was equilibrated by using a pseudo-isopiestic technique to form ultimately an aggregate of Ti_3AlC, Ti_2AlC and TiC phases. The aggregate was primarily composed of Ti_3AlC with minor amounts of Ti_2AlC and TiC, as determined by an X-ray diffraction analysis. The $Ti_3AlC/Ti_2AlC/TiC$ aggregate was subsequently oxidized at 1873 K to form a scale composed of an outer layer of Al_2O_3-TiO_2-Al_2TiO_5 with an inner layer consisting of TiO-Al_2O_3-Al_4CO_4. The measured scale thickness grew according to Wagner's parabolic growth rate, which estimates an effective diffusion coefficient of 6 $(10)^{-8}$ cm^2/s. The scale appears to grow with Ti ions migrating outward from the $Ti_3AlC/Ti_2AlC/TiC$ core and oxygen ions diffusing inwardly toward the core.

The transient temperature distribution of a cylindrical, carbide packed bed (i.e., B_4C) was simulated with COMSOL software to determine the response of the bed to a sudden temperature spike exposed to the outer wall of the bed. The temperature distribution of B_4C was similarly heated and compared with Hf and Zr metal. The thermal conductivity of Hf and Zr is higher than the B_4C packed bed and hence they respond quicker than B_4C. The packed bed still takes approximately 1200 s to plateau the temperature distribution between the cylinder surfaces to the centerline of the carbide packed bed of 5 cm diameter. Though the modeling of the distributions in the carbide packed bed gives an understanding of the transient heat response behavior driven by radiation, the effect of the plasma on the surface temperature of individual carbide particles needs further investigation to understand the plasma contribution to densification of a carbide packed bed.

Table of Contents

1. Introduction 3

2. Objectives and Statement of Work 4

3. Scientific and Technical Background for Motivation 5

3.1 Thermodynamic Considerations 5

4. Research Effort and Findings 6

4.1 Plasma-Surface Reactions 6

4.1.1 Plasma Matter 6

4.1.2 Plasma Temperature 6

4.1.3 Fundamental Plasma Components 7

4.1.4 Plasma-Surface Reactions 8

4.1.5 Development of adsorption/desorption equations 9

4.1.6 The Plasma-Surface Behavior 11

4.2 Experimental Considerations for the Synthesis of Ti_3AlC 14

4.2.1 Pseudo-isopiestic technique used for synthesis 14

4.2.2 Experimental Oxidations after Synthesis 14

4.3 Computational Analysis of Thermal Energy within B_4C 16

4.3.1 Configurations for Heat Transfer Simulations 16

4.3.2 Simulating Chemical Reactions 19

4.3.3 Results of Computational Analysis of Heat Transfer 20

4.4 Discussion of Plasma –Surface Reactions with Graphite or Carbides 23

5. Conclusions 24

6. Personnel Supported 25

7. References 25

1. Introduction

The plasma atmosphere can be useful for processing materials to change surface characteristics or apply coatings and for converting coal directly into power in a magnetohydrodynamic (MHD) generator operating at temperatures greater than 1873 K. In both cases, understanding the plasma-surface interactions along with the interfaces of phases (i.e., plasma/solid and plasma/liquid) is clearly needed. For plasma processing, the plasma can be categorized according to thermal and nonthermal plasma with the pressure of 10 kPa used as the dividing parameter. At pressures less than 10 kPa the electron and heavy particle temperatures are equivalent, as explained by Boulos, Fauchais and Pfender [1]. Whether the plasma is used or not, the materials must sustain temperatures greater than 1273 K. For example, Natesan and Bakker [2] described that slagging gasifiers may reach oxidizing atmospheres in the range of 10^{-21} to 10^{-10} atm when operating at temperatures from 1000 to 1700℃. As noted previously, MHD generators must use materials at temperatures greater than 1873 K and within a plasma atmosphere.

For coal gasifiers or air-breathing turbines, materials are needed to resist oxidation, sulfidation and carburization. High temperature alloys containing Cr, Al, and Si usually resist oxidation, because of an adherent, compact and stable scale consisting of Cr_2O_3, Al_2O_3 and SiO_2, as well as their spinels as reported by Kofstad [3] and Meier [4]. The vaporization of chromia by forming CrO_3(g) [5] may degrade or deplete the Cr_2O_3 scale, because its vaporization becomes a problem in flowing gas streams for temperatures greater than 1200°C. Alumina is thermodynamically more stable than either silica or chromia, as depicted in the established Ellingham diagram reported by Sigler [6]. Alumina scales generally resist oxidation better than Cr_2O_3 scales, but spallation and adherence of the oxide layer has continually created a challenge with the formation of wrinkles and convolutions, as reviewed by Wood and Stott [7].

Natesan and Bakker [8] reported that slagging gasifiers operating at temperatures from 1000 to 1700°C may reach oxidizing and sulfurizing atmospheres in the range of 10^{-21} to 10^{-10} atm and 10^{-8} to 10^{-4} atm, respectively. Although the focus of the research is on the plasma processing of materials used for oxidation resistance in coal gasifiers, one must also consider the performance of alloys in sulfurizing atmospheres. Sulfur causes a more aggressive degradation than with oxygen [9], because of the formation of sulfides, which usually have higher cationic diffusion rates. The significant demand for high temperature materials for sulfurizing atmospheres still exists, especially for coal conversion [9,10]. Though the material will be evaluated for oxidation resistance, the material must eventually survive a sulfurizing atmosphere and thus the reason for selecting alumina and rutile phases. Brady et al. [11] have reported on the advantages of an alumina and Ti oxides under a sulfurizing-oxidizing atmosphere. However, Ti oxidizes in several forms as thermodynamically calculated by using FactSage software and databases [12]. The stability diagram of the Ti-C-O shows that the Ti oxides may range from Ti_3O_5, including the Magneli phases (i.e., Ti_nO_{2n-1}), to the rutile phase (TiO_2) depending on the oxygen atmosphere within the gasifier, as shown in Figures 1 and 2. However, only two Magneli phases (i.e., $Ti_{10}O_{19}$ and $Ti_{20}O_{39}$) stabilize at 1973 K with Ti_2O_3, Ti_3O_5, and TiO_2 possible at approximately one atmosphere upon conferring with Waldner and Eriksson [13] analysis of the Ti-O system.

The computational study investigated the plasma processing of carbides for the ultimate development of adherent, dense scales such as Al_2O_3-TiO_2 systems toward oxidation resistance at 1700°C. The computational investigation analyzed the experimental parameters (e.g.,

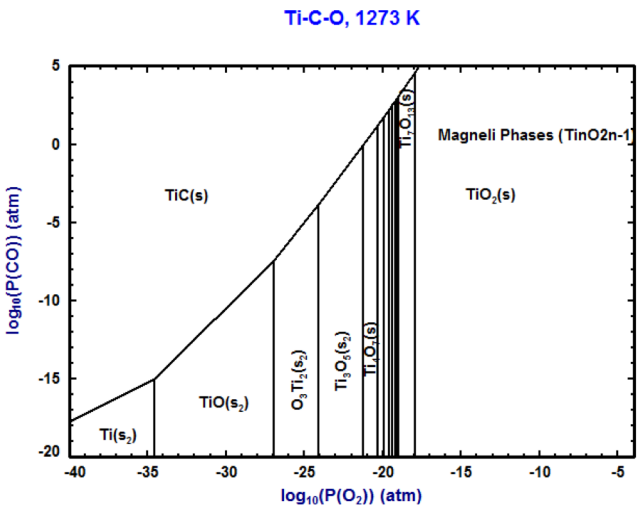

Figure 1 -- Ti-C-O Calculated Stability Diagram at 1273 K via FactSage 6.1

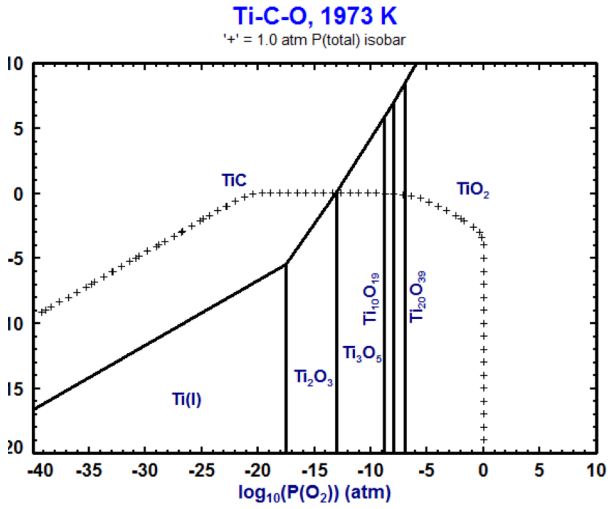

Figure 2 -- Ti-C-O Calculated Stability Diagram at 1973 K via FactSage 6.7

temperature) affecting the carbide particle surface, as well as to determine the mass and heat transport, within the carbide packed bed. With the computational framework developed for the investigation, the simulations of the plasma processing can be expanded in future research studies to other systems (e.g., ZrO_2-Y_2O_3, Hf-O-Ti-Y or MgO-Al_2O_3 systems), followed obviously with strategic experimentation.

In the following sections, the computational analysis of plasma-surface reactions is discussed with the strategic experimental study for acquiring Ti aluminate coatings after processing Ti-Al-C components under a controlled oxygen potential. A synopsis of the thermodynamic considerations for the high temperature materials is presented first, followed with a review of the plasma atmosphere possible above material surfaces. Afterwards, the computational analyses of the possible surface reactions are discussed. The strategic experimentation of the Ti-Al-C system is presented in terms of its processing and then the oxidizing behavior in air.

2. Objectives and Statement of Work

The goal of the proposed research was to investigate computationally the plasma processing with strategic experimentation of Ti_2AlC-TiC-Y_2O_3 packed beds, which ultimately will form Al_2O_3-Al_2TiO_5-Y_2O_3 scales. The processing of the composite and its oxidation involved the following research objectives:

- Investigate computationally the effects of the plasma on a carbide or oxide, which ultimately would impede oxygen ingress through the scale.

- Investigate the surface kinetics as a result of the plasma coupling with the surface reaction of the carbide.

3. Scientific and Technical Background for Motivation

3.1 Thermodynamic Considerations

The stability of the Ti and Zr oxides compared with the traditionally used Cr_2O_3 and Al_2O_3 scales are apparent when examining the Ellingham diagram, as shown in Figure 3. The thermodynamic software and databases from the HSC Chemistry version 7.0 were used [14]. Zirconia having the lowest Gibbs free energy indicates the most stable oxide from 1200 to 2300 K, though alumina is slightly above the Zr/ZrO_2 stability line. Although TiO stability approximates the ZrO_2 stability, TiO would probably form near the metal/scale interface as suggested from the stability diagram of Figure 1 and 2.

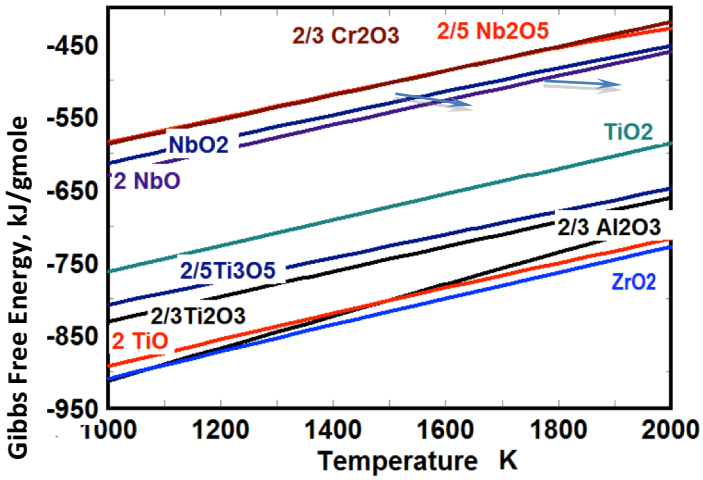

Figure 3 -- Ellingham diagram comparing Nb, Ti and Zr oxides with alumina and chromia (HSC Chemistry 7.0)

The development of an oxycarbide is exemplified by the Al-C-O system, which may form $Al_4CO_4/C/Al_2O_3$ triple point adjacent to graphite, as evident from Figure 4. Although the thermodynamic stability of alumina is comparable to zirconia as indicated from the Ellingham diagram, the alumina scale cracks during high temperature exposure. The scale grows laterally to form a wrinkling morphology, which subsequently spalls to expose the underlying metal. In studies [15–26] of the oxidation of Fe-Cr-Al alloys with and without Y, Hf and Zr additions, scale performance has been discussed to improve scale plasticity, segregants forming compounds to minimize oxygen ingress, and scale modifications to lower growth stresses. Hence, an alumina forming scale on an Fe-Cr-Al alloy would be extremely advantages if the wrinkling or the lateral growth could be controlled.

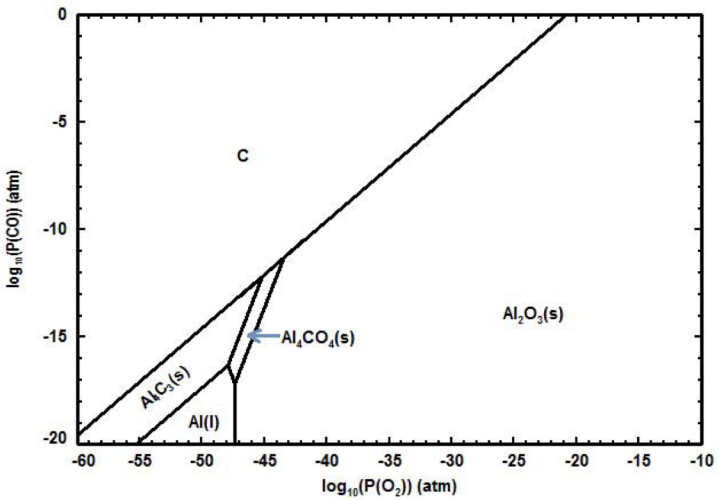

Figure 4 -- Stability diagram for the Al-C-O system at 1000 K via FactSage 6.1.

A Cr-Nb alloy has been suggested for high temperature such as reported by Brady and Tortorelli [27]. In addition, Nb may dissolve sufficiently into the Magneli phases to minimize the coefficient of thermal expansion between the Ti oxides or the formation of Nb_2TiO_7, as reported by Lashtabeg, Canales-Vazquez, Irvine and Bradley [28]. However, any Nb alloy must be completely isolated from the oxidizing atmosphere, because Nb does catastrophically oxidize at temperatures greater than 1473 K, as reported by Pasternak and Evans [29], Kofstad [30] and Park, Gokhale, Kumar and Abbaschian [31].

Rutile stabilizes the t-ZrO_2, evident when the ZrO_2-CaO, ZrO_2-MgO, ZrO_2-Y_2O_3 phase diagrams reported by Stubican [32] are compared with the ZrO_2-TiO_2 system [30]. Hence, with t-ZrO_2 stabilized by the rutile and possible formation of lower of Ti oxides (e.g., the Magneli phases) of Figures 1 and 2, their layered growth may minimize the oxygen ingress into the underlying alloy matrix, and if, their thermal expansion differences are not significant. For the Ti_2AlC-TiC-Y_2O_3, alumina or a titanate-aluminate may form with the former phase serving as a definite oxygen barrier.

4. Research Effort and Findings

4.1 Plasma-Surface Reactions

4.1.1 Plasma Matter

Plasma is referred to as the fourth state of matter, and it is estimated to constitute more than 99% of the visible universe [33]. Plasma is an ionized gas having at least one electron that is not bound to an atom or molecule, which converts the atoms or molecules into positively charged ions, as reported by Fridman [33]. He stated that plasma offers the following three major features attracting chemistry, physics and engineering:

1. Temperatures of at least some plasma components and energy density can significantly exceed those in conventional chemical technologies.
2. Plasmas are able to produce very high concentrations of energetic and chemically active species (e.g., electrons, ions, and radicals).
3. Plasma systems can essentially be far from thermodynamic equilibrium, providing extremely high concentrations of the chemically active species.

Plasmas can be categorized by the ratio of density of major charged species to that of neutral gas, called ionization degree. When the ionization degree is close to unity the plasma is said to be completely ionized plasma, but when the ionization degree is low, the plasma is called a weakly ionized plasma [33].

4.1.2 Plasma Temperature

The temperature in plasma, as in any gas results from the average energies of its neutral and charged particles and their related degrees of freedom. Plasma is said to be a multi-component system where various temperatures are exhibited. In electric discharges, which are common for plasma generated in laboratories, the energy from the electric field is accumulated by the electrons between collisions and, successively, transferred from the electrons to the heavy particles [33].

The energy from the electric field is transferred to the electrons during their mean free path, and through collisions with heavy particles only a small portion of that energy is lost since electrons are much lighter than heavy particles. The mass difference causes heavy particles to have initially a lower temperature than the electron temperature in plasma. Consequently, collisions of electrons with heavy particles called Joule heating equilibrate to their temperatures with sufficient time. Joule heating causes a temperature difference between electrons and heavy neutral particles in collisional weakly ionized plasma which is proportional to the square of the ratio of the electric field (E) to the pressure (p). The temperatures of heavy particles and electrons approach each other only in the case of small values of the E/p ratio meeting a basic requirement for local thermodynamic equilibrium (LTE) in plasma though restrictions on the gradients (e.g., temperature, mass and electric charge) may be required.

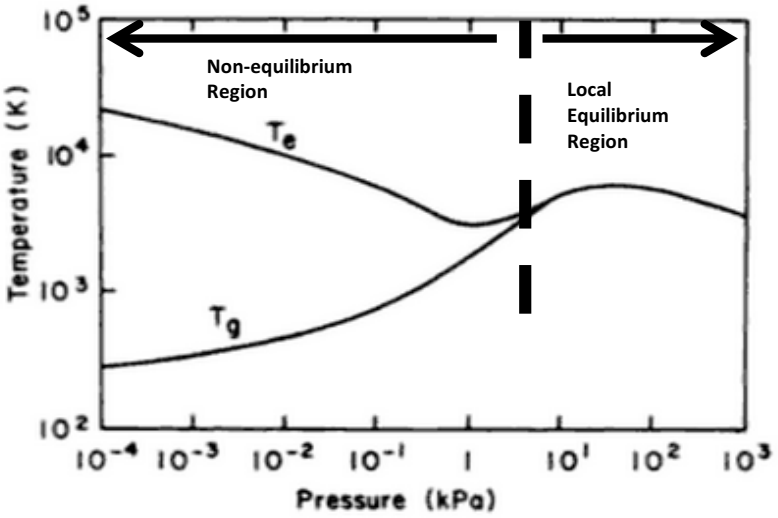

Figure 5 -- Plasma Temperatures-Pressures Boulos, Fauchais and Pfender [1].

Several plasmas occur very far from thermodynamic equilibrium and are characterized by multiple temperature ranges related to different plasma particles and different degrees of freedom. The electron temperature frequently surpasses that of the heavy particles (T_e>>T_g), as shown in Figure 5. In these non-equilibrium plasmas, the ionization and chemical processes are determined by electron temperature and are not so sensitive to thermal processes and the temperature of the gas. These types of plasmas are called non-thermal plasma. The plasmas where ionization and chemical processes are determined by temperature are called thermal plasma. Both thermal and non-thermal plasmas have many features in common but thermal plasmas are used in more powerful applications whereas non-thermal plasmas are used in more selective applications.

4.1.3 Fundamental Plasma Components

Each component of chemically active plasma plays a particular role in plasma-chemical kinetics in the multi-component system. These components make a plasma highly reactive due to the large concentrations of charged particles such as electrons, negative and positive ions, excited atoms and molecules resulting from electronic and vibrational excitation [33]. The energy from the electric field is first received by the electrons and then distributed between other components and specific degrees of freedom. Altering parameters of the electron gas such as temperature, electron energy distribution function or density permits control and optimization of plasma-chemical processes.

Due to their high energy and their ability to suppress activation barriers of chemical reactions, the charged heavy particles or ions can make a significant contribution to plasma-chemical kinetics. The highest values of energy efficiency can be reached through vibrational excitation. Another type of excitation of atoms and molecules is electronic excitation and can play a significant role when the lifetime of the excited particles is quite long.

Often, plasma is not only a multi-component gas, but also a very non-equilibrium system. The active species concentrations can surpass those of quasi-equilibrium systems by many orders of magnitude at the same gas temperature. When successfully controlled, plasma allows chemical processes to be directed in the desired and optimized direction [34].

In quasi-neutral plasmas the number densities of electrons and the positive ions are usually equal; however, in electronegative gases such as O_2 with high electron affinity, negative ions also form. Energy is transmitted from the electrons in plasma, which acquire the energy from the electric fields to the other components because of their high mobility. The rates of such processes depend on the number of electrons with sufficient energy to proceed. The probability density for an electron to have energy ϵ can be termed by means of the electron energy distribution function (EEDF), or $f(\varepsilon)$, which is mostly determined by the electron temperature T_e and usually described by the quasi-equilibrium Maxwell-Boltzmann distribution function:

$$f(\varepsilon) = 2\sqrt{\varepsilon/\pi(kT_e)^3}\exp\left(-\frac{\varepsilon}{kT_e}\right) \tag{1}$$

where k is the Botlzmann constant (k=1 when temperature is given in energy units). The mean electron energy proportional to temperature in this case can be expressed as:

$$\langle\varepsilon\rangle = \int_0^\infty \varepsilon f(\varepsilon)d\varepsilon = \frac{3}{2}T_e \tag{2}$$

In most plasmas, the mean electron energy is from 1 to 5 eV.

Both elastic and inelastic collisions occur in plasmas. In elastic collisions the internal energies of colliding particles do not change and the total kinetic energy is conserved. In inelastic collisions such as ionization, the energy transfers from the kinetic energy of colliding particles into internal energy [33].

4.1.4 Plasma-Surface Reactions

A large number of variables are present in plasmas and some parameters have been established by trial and error development. This is why plasma modeling has gained importance as a tool to reduce time and cost compared to experimentation. The understanding of surface reactions is vital for the development of these new tools.

An important contribution of plasma in material's processing has been in etching processes. Early studies by IBM greatly contributed to achieve highly directional etching [35]. Although plasma etching has been successful, the process is not easily controlled due to complexity of neutral radicals, positive ions, and ultraviolet (UV) photons that interact simultaneously with the

substrate's surface. Atomic and molecular radicals are produced predominately by electron impact and dissociative attachment reactions. The balance between formation and loss reactions in the plasma determines the radical number densities.

Most of the important reactions in plasma etching take place on the walls of the chamber or on the material surfaces due to diffusion becoming faster at lower pressure. Even when higher pressures are used such as in plasma-enhanced chemical vapor deposition (CVD), association reactions for atoms and small molecules are likely to be slow in the gas phase and are more probable to occur on a surface. A potential drop is introduced in the plasma sheath, which is a thin region of net positive charge near the boundaries of the plasma, though the sheath accelerates positive ions towards the walls [36]. Kota, Coburn, and Graves [37] report that recombination reactions such as:

$$X + X \xrightarrow{\text{surface}} X_2 \tag{3}$$

are important in determining the gas-phase concentrations in reactors and ultimately the scale level. Lee et al.[38] studied the gas-phase kinetics and plasma chemistry of high density oxygen discharges. As molecular oxygen (O_2) enters an ionized system, the molecules collide with electrons and undergo electronic transitions and form O_2^+, O^-, O and O^*. According to Lee et al., free radicals ionize further to form O^+ with the positive ions drifting to the walls and are recycled back to the plasma as neutrals upon neutralization with electrons to end as O. Coupling this finding with work cited below helps to prove that oxygen adsorbed on surface sites sets the rate determining step for plasma surface reactions, where the oxygen adsorbs onto a site, diffuses until it recombines with another oxygen atom to form an O_2 molecule, and finally desorbs from the surface.

Kurunczi, Donnelly and Guha [39] studied surface reactions and kinetics of oxygen in a plasma atmosphere by using the spinning wall method. The method used a coated cylindrical substrate that can be rotated at a rate of up to 200,000 rpm with a specific point on the surface exposed to a plasma. The approach allowed the study of adsorption/desorption of oxygen on the surface of the substrate as quick as 150 μs. For the present study, results from Kurunczi et al.[39] were used to explain the effects of plasma on the surface reactions of oxygen on an aluminum surface.

4.1.5 Development of adsorption/desorption equations

Wang et al. [40] studied the oxidation of a TiAlNb intermetallic which involved dissociative adsorption of oxygen similar to the gas-metal reactions of metals as reviewed by Grabke and Horz [41]. For a broader view of Al2O3 scale formation, which is expected with metals containing significant Al content and forming an alumina scale, it develops from the following reaction sequence:

$$O_2 + 2V = 2O_{ad} \tag{4}$$

$$Al + O_{ad} \rightarrow AlO \tag{5}$$

$$AlO + O_{ad} \rightarrow AlO_2 \tag{6}$$

$$AlO_2 + O_{ad} \rightarrow AlO_3 \quad (7)$$

The sequence above incorporates dissociative adsorption of oxygen where the O_2 initially dissociates when adsorbed onto two surface sites V and AlO_3 which is formed when the adsorbed oxygen O_{ad} reacts with Al, AlO, and AlO_2 consecutively.

The reaction rates (r_i) for these reactions are:

$$r_{O,ad} = k_1 p_{O_2} V^2 - k_1' C_{O,ad}^2 \quad (8)$$

$$-r_{Al} = k_2 a_{Al} C_{O,ad} \quad (9)$$

$$r_{AlO} = k_2 a_{Al} C_{O,ad} - k_3 C_{AlO} C_{O,ad} \quad (10)$$

$$r_{AlO_2} = k_3 C_{AlO} C_{O,ad} - k_4 C_{AlO_2} C_{O,ad} \quad (11)$$

$$r_{AlO_3} = k_4 C_{AlO_2} C_{O,ad} \quad (12)$$

where k_i is the forward rate constant, k_1' is the backward rate constant, p_{O_2} is the oxygen partial pressure, C_i the concentration of each species, and a_{Al} the activity of aluminum on the alloy surface.

Equation (4) is the rate determining step of oxygen adsorption with its rate equation of (8), and the steady-state condition for the adsorbed oxygen and its consumption is:

$$r_{O,ad} = r_{AlO} + r_{AlO_2} + r_{AlO_3} \quad (13)$$

The series parallel reactions for the single, double and triple binding of oxygen with aluminum is included in the consumption, resulting in:

$$k_1 p_{O_2} V^2 - k_1' C_{O,ad}^2 = k_2 C_{O,ad} a_{Al} + k_3 C_{O,ad} C_{AlO} + k_4 C_{O,ad} C_{AlO_2} \quad (14)$$

Solving equation (14) for V results in:

$$V = [k_1' C_{O,ad}^2 + k_2 C_{O,ad} a_{Al} + k_3 C_{O,ad} C_{AlO} + k_4 C_{O,ad} C_{AlO_2} / k_1 p_{O_2}]^2 \quad (15)$$

Substituting equation (15) into equation (8) (rate of formation of O_{ad}) the rate equation develops:

$$\frac{1}{S}\frac{dC_{O,ad}}{dt} = C_{O,ad}\alpha \quad (16)$$

where S is surface area, and $\alpha = k_2 a_{Al} + k_3 C_{AlO} + k_4 C_{AlO_2}$.

Integrating from the initial adsorbed oxygen ($C_{O,ad}^i$) to the final adsorbed oxygen ($C_{O,ad}^f$), the subsequent ratio for adsorbed oxygen becomes:

$$\ln\left[\frac{C_{O,ad}^f}{C_{O,ad}^i}\right] = S\alpha t \quad (17)$$

The ratio of the rate of oxygen adsorption to the rate of AlO_3 formation can then be acquired to determine the concentration with respect to the oxygen potential p_{O_2}:

$$\frac{r_{O,ad}}{r_{AlO_3}} = \frac{\frac{2}{S}\frac{dp_{O_2}}{dt}}{\frac{1}{S}\frac{dC_{AlO_3}}{dt}} = \frac{k_2 C_{O,ad} a_{Al} + k_3 C_{O,ad} C_{AlO} + k_4 C_{O,ad} C_{AlO_2}}{k_4 C_{AlO_2} C_{O,ad}} \quad (18)$$

For reactions (12)-(13) which achieve equilibrium, $r_{AlO} = r_{AlO_2} = 0$ at steady state, equation (18) becomes:

$$\frac{2dp_{O_2}}{dC_{AlO_3}} = \frac{k_2 C_{O,ad} a_{Al} + k_3 C_{O,ad}\left[\frac{k_2 a_{Al}}{k_3}\right] + k_4 C_{O,ad}[\frac{k_2 a_{Al}}{k_4}]}{k_4 C_{O,ad}[\frac{k_2 a_{Al}}{k_4}]} \quad (19)$$

The AlO_3 concentration (C_{AlO_3}) with respect to Langmuir (L), which is the product of vacuum (in 10^{-6} Torr) and time (in second), was acquired by combining equation (17) and equation (19) to give equation (20):

$$\frac{dC_{AlO_3}}{dL} = \frac{2}{3}\left[\frac{S\alpha t}{\ln (C^f_{O+,ad}/C^i_{O,ad})}\right] \quad (20)$$

which incorporates the rate-determining step of a dissociative adsorption of oxygen and was found to be consistent with the initial oxidation rate of the Ti-44Al-11Nb intermetallic.

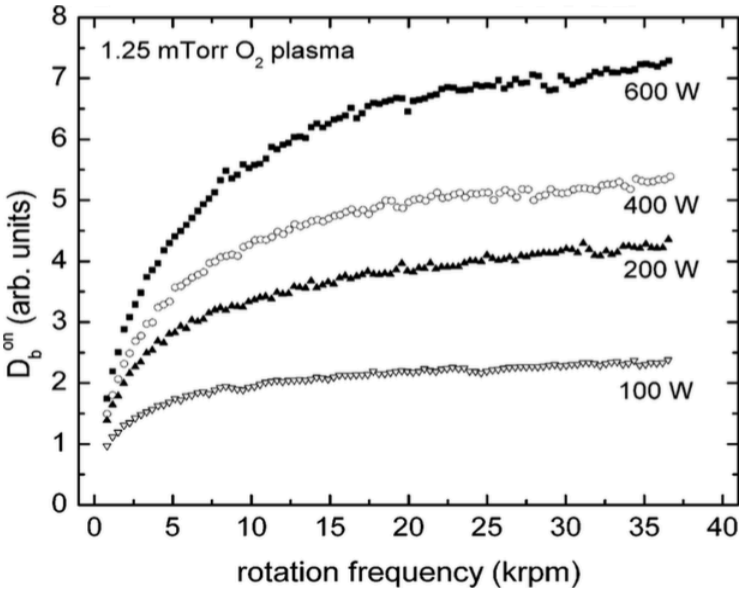

Figure 6 -- Adsorption of O_2 vs the substrate rotation frequency for a 1.25 mTorr O_2 plasma as a function of power [42].

4.1.6 The Plasma-Surface Behavior

Kurunczi, Guha and Donnelly [42] used a "spinning wall" technique to study the recombination of oxygen atoms on an anodized aluminum surface in an oxygen plasma atmosphere. They used a rotating cylindrical wall of a plasma reactor to expose the surface to oxygen plasma and then to a differentially pumped mass spectrometer (MS) linked to Auger electron spectroscopy. Desorption of O_2 was reported and the only plausible explanation according to Kurunczi, Guha, and Donnelly is the recombination of O atoms. Measurements of O_2

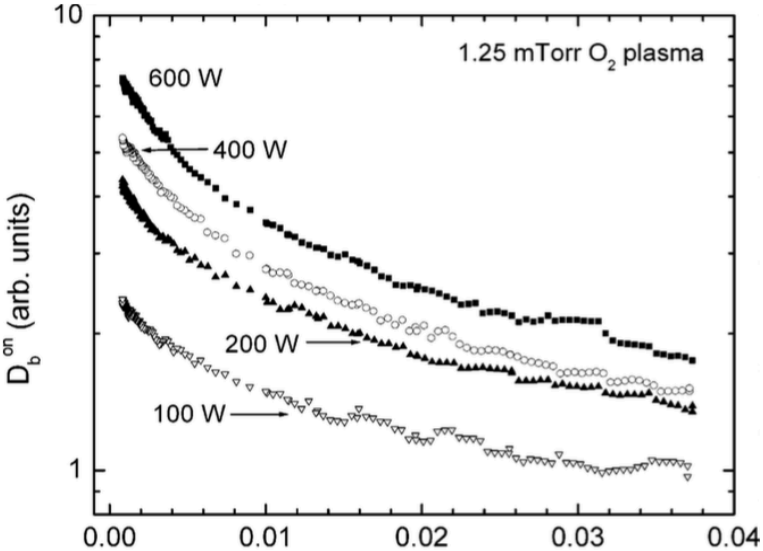

Figure 7 -- Desorption of O_2 vs reaction time for a 1.25 mTorr O_2 plasma, as a function of power [42]

adsorption versus rotation frequency at a constant pressure of 1.25 mTorr were plotted as functions of power as shown in Figure 6. The desorption of O_2 content decays logarithmically with increasing time, as a function of power for 1.25 mTorr and shown in Figure 7.

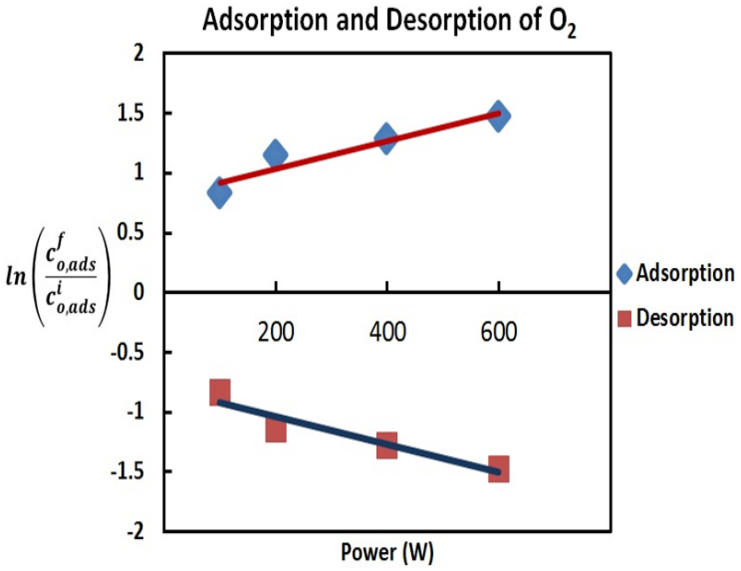

Figure 8 -- Adsorption and desorption of O_2 as a function of power as determined by using the adsorption ratio of Eq. (23) with data from Figures 6 and 7.

In the model formulated by Kurunczi, Guha and Donnelly [39], they assumed that adsorption of oxygen happens at surface sites, then oxygen detaches from these sites and becomes mobile, diffusing after along the surface to react with adsorbed oxygen which leads to recombination and desorption of O_2. The contribution of O_2^+ and O^+ was discarded for the formation and desorption of O_2 from anodized Al. Kurunczi et al. [39] used the following reactions to show O atoms adsorbing at vacant surface sites from O_2 plasma by a Langmuir-Hinshelwood (L-H) process, and recombining in a second-order reaction:

$$O_g + V = O_{ad} \qquad (21)$$

$$2O_{ad} \rightarrow O_{2(g)} + 2V \qquad (22)$$

One should add that the L-H process usually applies to surfaces at approximating room temperature. In an extended temperature range, the sequence of reactions (4) to (7) is not limited to temperatures near 300 K.

Though reaction (4) was devised for adsorption on the Ti-44Al-11Nb intermetallic, the desorption of oxygen is expected to occur as the backward reaction sequence starting with the decomposition of AlO_3 from reactions (7) to (4). The similarity in reactions (4) and (21) are apparent considering the former adsorption/desorption characteristics

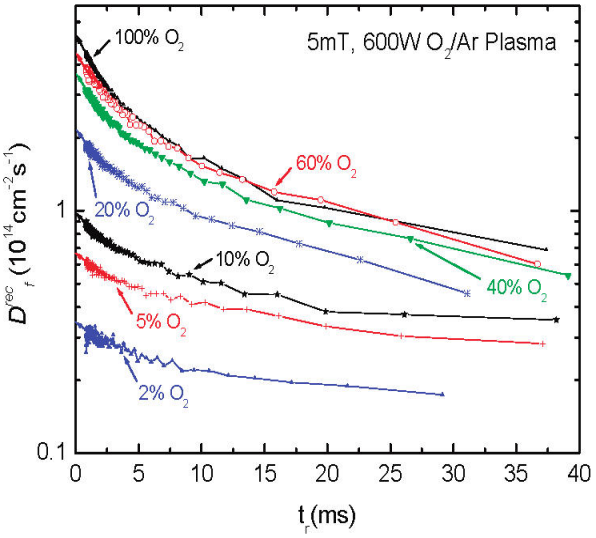

Figure 9 -- Net desorption flux of O_2 atoms as a function of time at different p_{O2} in an O_2/Ar plasma, as reported by Guha et al. [43].

of reaction (4). The difference in adsorption and desorption rates may be apparent if the function with respect to oxygen potential dramatically diverges beyond just a negative slope, as apparent in the Figure 8.

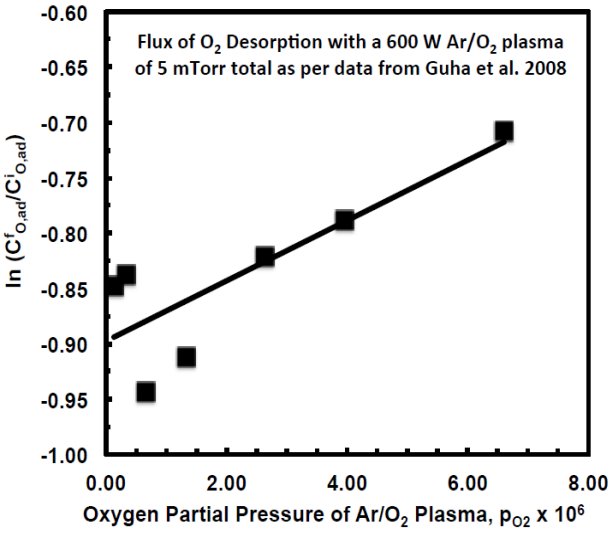

Figure 10 -- Effect of gaseous oxygen potential on adsorbed oxygen with a 600 W Ar/O_2 plasma of 5 mTorr total as per data from (Guha, Kurunczi, Stafford, Donnellhy, & Pu, 2008).

Guha et al.[43] observed the recombination of oxygen atoms on an anodized aluminum surface at room temperature in a plasma atmosphere also with the spinning wall method mentioned earlier. The results show that decaying desorption flux continue to drop with time. After a short time, a fast rate of desorption exists which indicates that a majority of surface sites have low binding energy. Figure (10) was obtained from Figure 9, showing desorption flux of O_2 formed by O atoms recombining as a function of reaction time at different oxygen partial pressures in the feed gas mixture of an O_2/Ar plasma at 5 mTorr and 600 W.

The results from Kurunczi, Guha, and Donnelly [42] who also used a spinning cylindrical electrode to measure the recombination of oxygen atoms were interpreted differently with adsorption, as well as desorption of oxygen plot were reproduced as a function of oxygen potential (p_{O_2}). Figure 8 was made by combining Figure 6 and Figure 7 to show adsorption and desorption of O_2 as a logarithmic ratio of final to initial oxygen concentration with respect to power. The graph shows adsorption and desorption mirroring each other, as adsorption increases or desorption decreases.

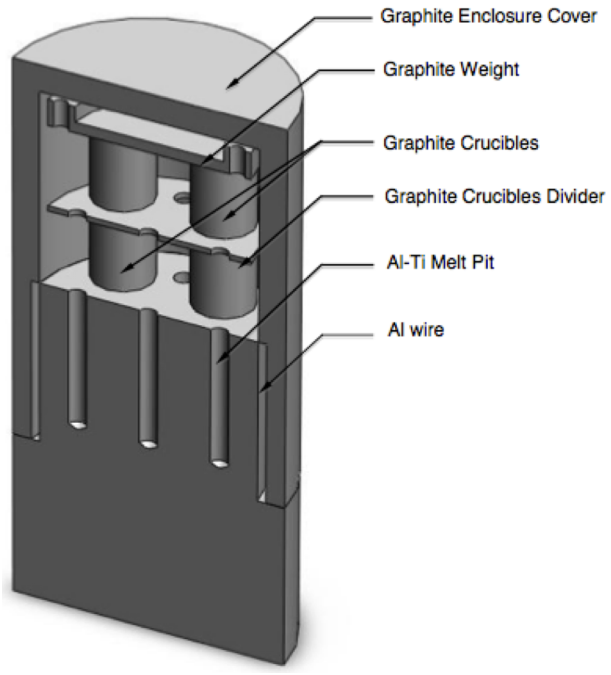

Figure 11 -- Sketch of pseudo-isopiestic system to control oxygen potential.

The key reaction is still the adsorption of oxygen which is the rate determining step. By coupling this rate determining step with the surface temperature distribution on the carbide substrate, the O_2 within the gas will react with the carbon atoms to ultimately form CO.

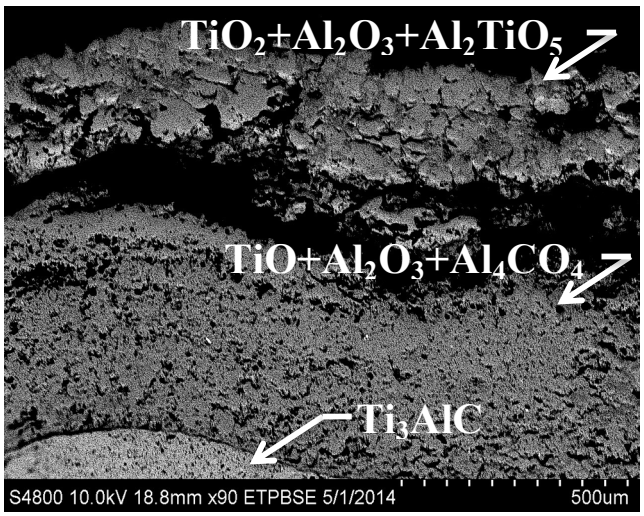

Figure 12 -- Scanning electron microscope microstructure after oxidizing a Ti_3AlC synthesized within a pseudo-isopiestic thermodynamic system.

4.2 Experimental Considerations for the Synthesis of Ti_3AlC

4.2.1 Pseudo-isopiestic technique used for synthesis

In a parallel research thrust, a pseudo-isopiestic technique was used to synthesize Ti_3AlC by controlling the oxygen potential in a closed, thermodynamic system. The pseudo-isopiestic system was designed with machined graphite rods to form a graphite enclosure inserted onto a graphite pedestal, which was subsequently sealed with liquid Al isolating the graphite crucibles, as shown in Figure 11. On one end of the system, its temperature of 1000 K melts Al subsequently reacting with graphite to form a triple point of $Al/Al_4C_3/Al_2O_3$, which sets the oxygen potential (p_{O_2}) at 10^{-47} atm, as evident in the Al-C-O stability diagram of Figure 4. Titanium was also added to Al to cause cracking of the alumina film as the Al melts exposing it to the gas phase. At the other end of the graphite enclosure, a temperature of 1700°C was attained and equilibrated a 39Ti-14Al-47TiC (in wt%) mixture with Al wire, Ti pellets and TiC powder of 10 μm contained in graphite crucibles. The entire graphite pseudo-isopiestic system was placed in an alumina tube through which deoxidized Ar at 1 mL/s was injected to minimize the oxidation of the graphite. After equilibrating the Ti-Al-TiC mixture for more than four hours, Ti_3AlC with TiC and Ti_2AlC formed as determined by x-ray diffraction, though a minor intensity peak of Ti_3Al was apparent. The three-phase field of Ti_3AlC, Ti_2AlC and TiC does occur at a carbon content slightly greater than the Ti_3AlC compound but at a lower content the two-phase field of Ti_3AlC-Ti_3Al exists, as indicated by the Ti-Al-C phase diagram by Bandyopadhya, Sharma and Chakraborti [44].

4.2.2 Experimental Oxidations after Synthesis

The Ti_3AlC was subsequently oxidized from 5 to 60 minutes. The microstructure indicated a duplex scale develops – the outer layer is a mixture of TiO_2, Al_2O_3 and Al_2TiO_5 as shown in Figure 12. The inner layer indicating TiO, Al_2O_3 and Al_4CO_4 surrounds the inner core of Ti_3AlC. However, more material analysis is needed, because we sometimes found Ti_3O_5 on the x-ray diffraction pattern.

In analyzing the oxide scale further, a plot of the oxide thickness with the square root of time suggests a diffusional control of the oxidation though data is scattered around the least square line, as shown in Figure 13. Each point represents an average of at least four measurements though the value for 60 minutes (or $\sqrt{t} = 7.7$) was an average of five oxide thicknesses.

With the assumption of Wagner's parabolic growth rate, the slope of the least square line gives an effective diffusion coefficient according to the following equation:

$$D_{eff} = \frac{k_p}{\int_{p_{O_2}^i}^{p_{O_2}^o} dlnp_{O_2}} \qquad (23)$$

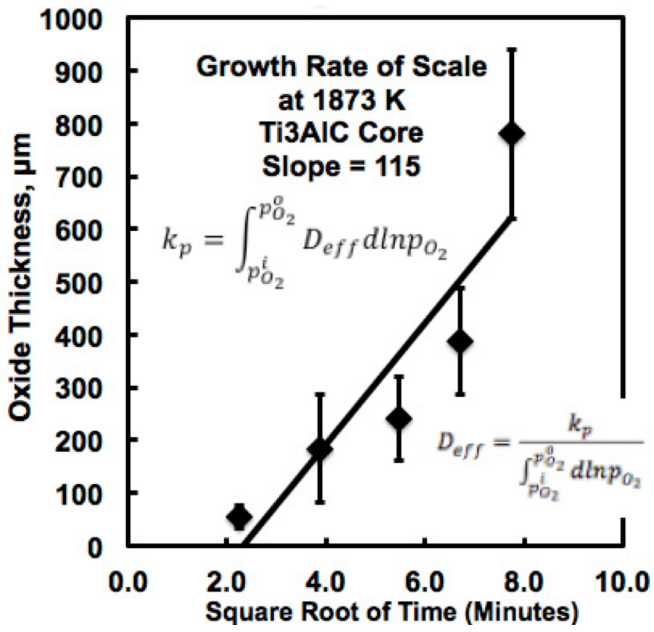

Figure 13 -- Scale thickness from Ti_3AlC core to outer surface after oxidization in air 1873 K.

The equation uses the parabolic rate constant, usually referred as the practical rate constant, k_p (cm^2/s), the oxygen potential difference resulting from the $p_{O_2}^i$ established at core/scale interface and the $p_{O_2}^o$ at the scale/gas interface. The practical rate constant is easily converted to Wagner's gravimetric rate constant, kg ($g^2cm^{-4}s^{-1}$), by using the density of the scale, so in our case the density of alumina, $\rho_{Al_2O_3}$, gives the following equation:

$$k_g = 2k_p\rho_{Al_2O_3}^2 \qquad (24)$$

If the rate determining diffusion occurs through a dense alumina scale, the effective diffusion (D_{eff}) equals $2.5x10^{-13}$ cm^2/s as calculated by Ramanarayanan et al. [19]. However, from the plot of Figure 13, the $D_{eff} = 6.2x10^{-8}$ cm^2/s. The faster effective diffusion acquired from the plot than the $2.5x10^{-13}$ cm^2/s suggests that the Ti oxide phase also contributes to the scale development. The oxidizing trend may mask an inner rate initially controlled by Ti ions migrating outward and the outer scale controls the oxygen diffusing inwardly as the scale grows. A thermodynamic analysis of the effect of the oxygen potential on

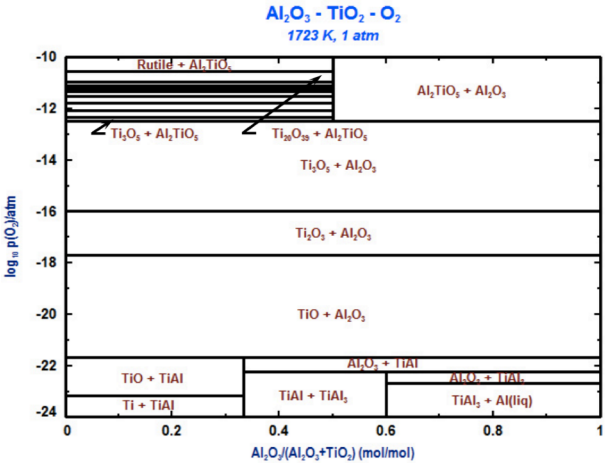

Figure 14 -- Calculated Al_2O_3-TiO_2 phase diagram as a function of oxygen potential at 1723 K, as determined by FactSage version 6.1.

Al_2O_3-TiO_2 system indicates that the Ti_2O_3 and Ti_3O_5 are stable with Al_2TiO_5 forming at a $p_{O_2} > 10^{-12.5}$ atm, as shown in the phase diagram of Figure 14. The diagram agrees with Muan and Osborn [45] evaluation of the Al_2O_3-TiO_2 system in which limited solubility exists among the phases of Al_2O_3 and TiO_2 in Al_2O_3•TiO_2.

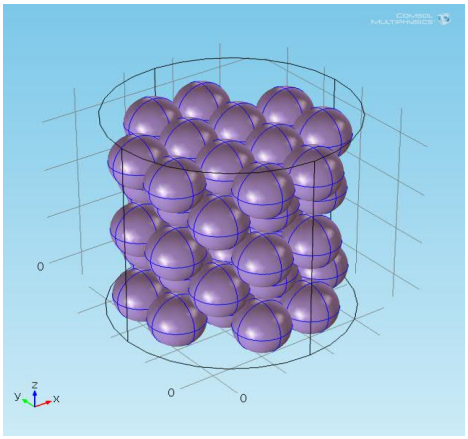

Figure 15 -- B_4C packed bed represented as spheres (COMSOL).

4.3 Computational Analysis of Thermal Energy within B_4C

4.3.1 Configurations for Heat Transfer Simulations

Simulations for the plasma-surface reactions were separated into plasma reactions, Ti carbide experiments and heat transfer calculations instead of a combined study of plasma-surface reactions at temperatures greater than 1873 K to ease the calculating capital as well as to understand the divided sections of the study. The simulation of heating a packed bed of a carbide, specifically B_4C, particles was the first part of this work. Boron carbide powder heated to 1700 ℃ contains particles with an average size of 10 µm, and pores that can vary from 1 to 10 µm. Replicating the irregular morphology of the B_4C powder for modeling would have increased the computing time needed to solve the simulations, so even though it was a big jump, spheres were chosen to represent the packed bed geometry shown in Figure 15.

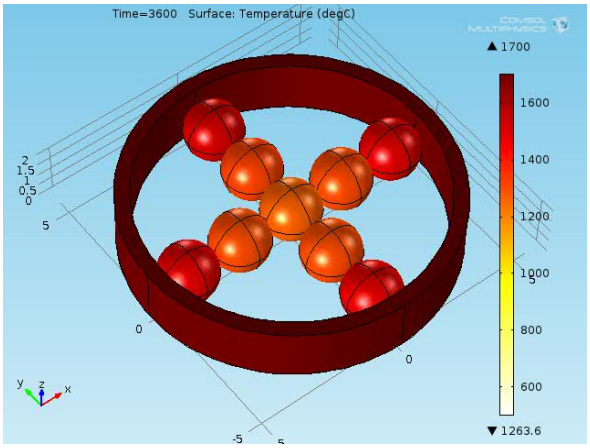

Figure 16 -- Initial B_4C packed bed heat transfer simulation (COMSOL).

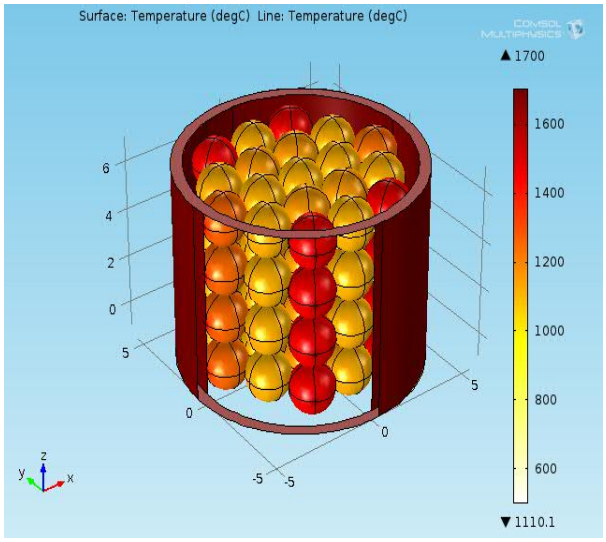

Figure 17 -- Addition of B_4C spheres to geometry (COMSOL).

Initially, placement of the spheres proved challenging, because the software would indicate the boundaries were intersecting each other and would fail to create a valid mesh. COMSOL has a CAD feature with a graphical user interface, which facilitates creating a model, though difficult with building complex geometries [46].

Different approaches were attempted to have a closely-packed packed bed. Since the model was represented by a symmetrical cylinder, as can be seen on Figure 17 only half of the geometry was modeled to use less computing memory, and even a model representing only one sixth of the geometry was modeled, as shown in Figure 18. However, modeling so many spheres proved to increase significantly the computing time. It was not certain the model accounted for losses with the new configuration, so a traditional full geometry was brought back. To ensure that the spheres were touching each-other without intersecting; spheres were placed by creating one row of spheres with the coordinates of each sphere's center. Then, the row was duplicated and placed at an angle which varied depending on the number of rows needed, as shown in Figure 19.

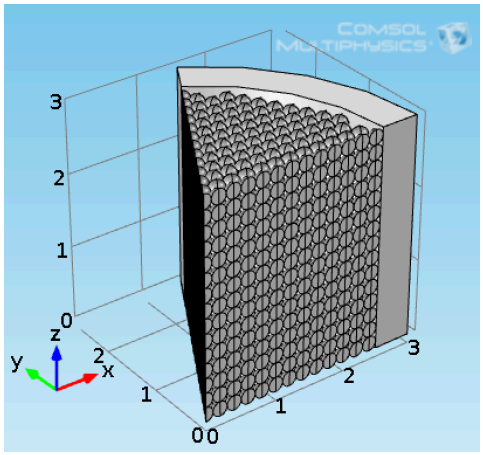

Figure 18 -- One sixth of B_4C packed bed (COMSOL).

The simplified model was used to test the capabilities of COMSOL. Conduction and convection were included in the model, where the outside cylinder represents a graphite crucible being heated at the walls as an initial condition. An experimental equivalent for the system heated instantly was configured with a crucible containing a boron carbide powder inside an induction furnace. The current passing through a coil would create an electromagnetic field, where the electromagnetic waves would instantly heat up the specimen upon contact.

To simplify the simulations, the electromagnetic field was removed by modeling the heating of a packed bed of B_4C particles within

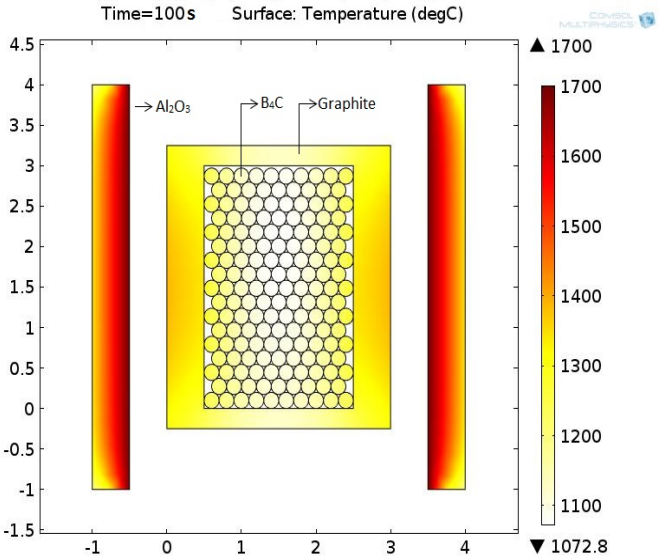

Figure 19 -- Temperature distribution of B_4C contained in a graphite crucible after 100 s (COMSOL).

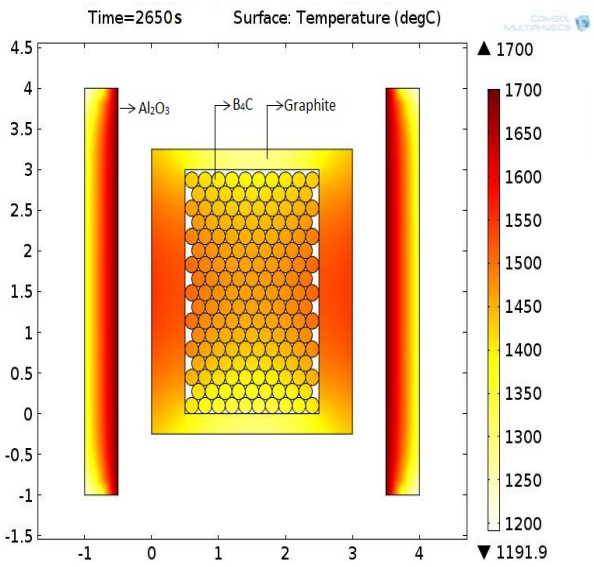

Figure 20 -- Temperature distribution of B_4C contained in a graphite crucible after 2650 s (COMSOL).

$MoSi_2$ furnace at 1700°C. An alumina cylindrical wall was assumed inside a furnace and a graphite cylindrical crucible containing the packed bed was placed inside the alumina cylinder. The inner, alumina cylinder wall with a temperature of 1700°C radiated the heat onto the graphite crucible enclosing the B_4C spheres to identify the time needed for the packed bed to reach steady-state condition 100 and 2650 s, as shown in Figures 19 and 20, respectively.

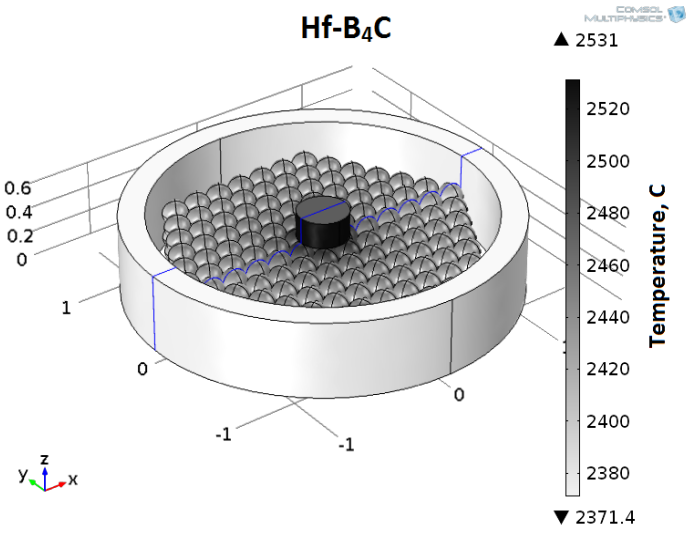

Figure 21 -- Configuration of a Hf or Zr metal disc on B_4C spheres used to simulate the heat transfer of liquid alloy on a B_4C packed bed (COMSOL).

A second model was then created to account for all three types of heat transfer, conduction, convection and radiation since the previous model was not completely coupled with radiation. Figure 21 represents a B_4C packed bed within a $MoSi_2$ furnace as well. The packed bed was mimicked in COMSOL by using spheres to represent the B_4C particles. The new configuration includes more spheres than in the past model. A graphite cylindrical wall was located inside a furnace with a temperature of 1700°C was assumed and then the packed bed immediately placed inside the graphite cylinder. The next step was to simulate the temperature profile as hafnium and zirconium metals melt, which initially started as a cylindrical disc, and react with boron carbide, as shown in Figure 21. The model included radiation in participating media with the addition of surface to surface radiation. A graphite cylinder held boron carbide spheres while a Hf disc was placed on top. The crucible was modeled as a cylinder with 3 cm outer diameter and 2.6 cm inner diameter. The B_4C particles were represented by 0.2 cm diameter spheres. The Hf cylinder had a diameter of 0.4 cm represented by a total of 254 spheres with two layers of boron carbide. At time zero, the entire geometry was set to

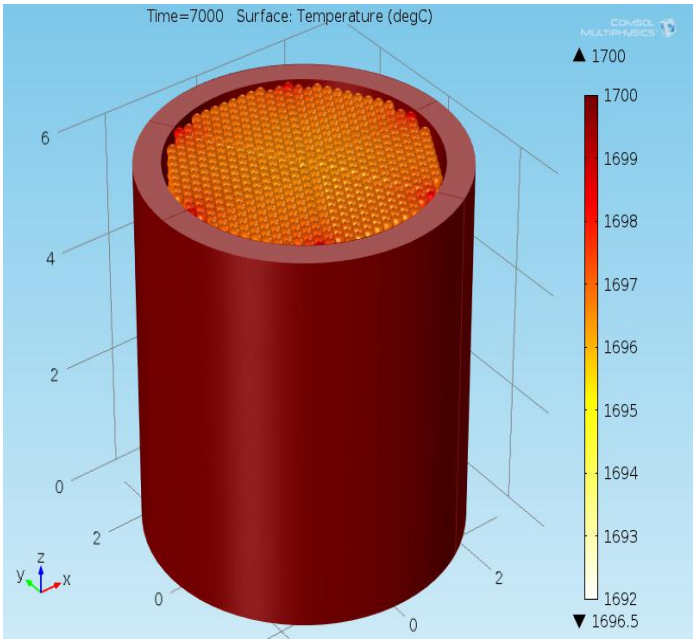

Figure 22 -- 3-Dimensional view of spheres mimicking B_4C packed bed (COMSOL).

25℃ with the exception of the outer crucible walls which were set to 2231℃ in order to calculate the time needed to reach a linearized temperature profile across a packed bed. After the temperature of the hafnium disc reached 2231℃, a 300℃ spike simulating an exothermic reaction between molten Hf and the B_4C was modeled.

An additional simulation was performed with the same model, only this time, a Zr disk replaced Hf. The system used the melting temperature of Zr of 1855℃ as a boundary condition on the outer crucible wall until equilibrium was reached. Then, the metal melted and created the temperature spike in the middle of the packed bed releasing heat. The temperature profiles of the B_4C, Zr and Hf will be shown in section 4.3.3, as well as the temperature profiles at the centerline to indicate the time needed for achieve steady-state condition for heat transfer.

4.3.2 Simulating Chemical Reactions

A model for oxidation was developed following the reactor with an injection needle model in COMSOL. Partial mixing was observed in the main channel before flowing through a packed bed, which produced a third species, TiO_2 (C). Temperature was set as a global parameter of 1700℃. The reaction rate constant was then defined as follows:

$$k = A\exp\left[\frac{-\Delta E}{RT}\right] \tag{25}$$

where A=0.980 $\frac{m^3}{(s\cdot mol)}$, ΔE=14145 $\frac{J}{mol}$, R=8.314 (kJ/(kmol-K), universal gas constant), and T=1700°C. The parameters were deduced by using the Gibbs free energy of reaction for the Ti/TiO_2 equilibrium, which determines the corresponding equilibrium constant then assumed as the rate constant, k.

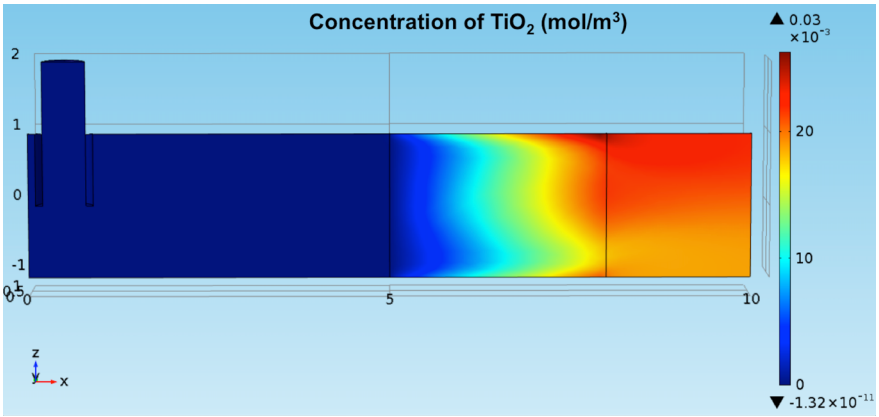

Figure 23 -- The concentration of TiO_2, the product, after Ti reacts with O_2 (COMSOL).

The flow through the main tube was modeled with the Navier-Stokes equations and the packed bed domain included the Brinkman equation, an extension of the Navier-Stokes equations. To use the Brinkman equation, the porosity of 30% and permeability of 1.9×10^{-9} m^2 for the packed bed were assumed. The mass transport properties were defined through diffusion and convection with chemical reaction kinetics. A reaction node

was used to account for the consumption of Ti and O_2 and the production of TiO_2 by using the reaction rate variable defined earlier with the concentrations of Ti and O_2. Concentrations for each reactant species were defined in the inflow nodes as well as diffusivity, which were defined in the transport properties node.

A hybridized mesh, which can use different elements, was best suited for simulations that included fluid flow and mass transport. In this simulation, a boundary layer mesh was used to resolve the field close to the walls, and a free tetrahedral mesh was used to solve the field elsewhere.

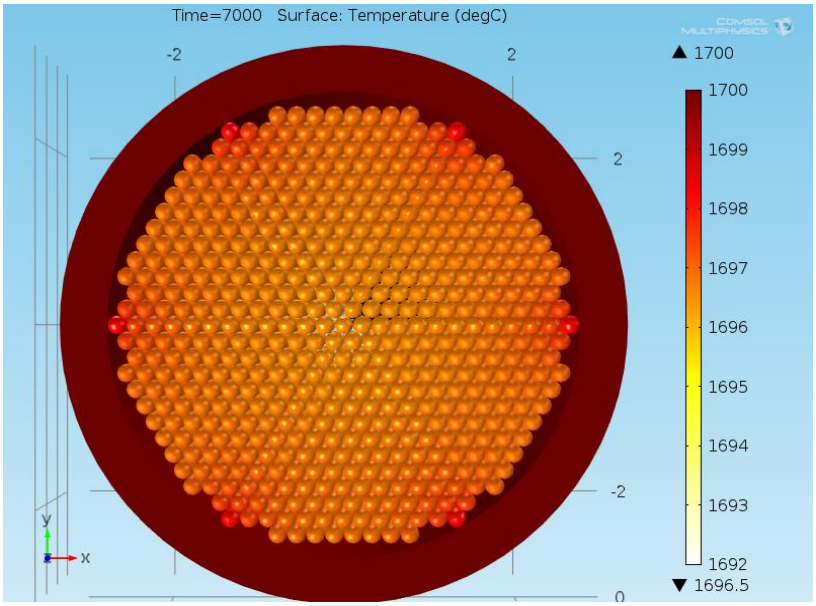

Figure 24 -- Top view of sphere configuration to simulate a packed bed (COMSOL).

4.3.3 Results of Computational Analysis of Heat Transfer

A B_4C packed bed contained in a graphite crucible was simulated inside placed a $MoSi_2$ furnace with the configuration shown in Figure 23. The temperature distribution after 100 s is depicted in Figure 24. It took approximately 2460 s for the B_4C to reach 1700°C though the spheres located in the interior were cooler, as shown in Figure 24. The temperature along the centerline lagged the outer wall. The radiative heat transfer should be considerably greater than the convective heat transfer at 1700°C. Still, it had to be ensured that the radiative/convective ratio was accurate on next simulations. The contribution of radiation at temperatures greater than 1000 °C was expected to significantly increase, because of the obvious T^4 term found in radiative heat transfer. Further examination was needed to correct the lack of coupling with radiative heat transfer,

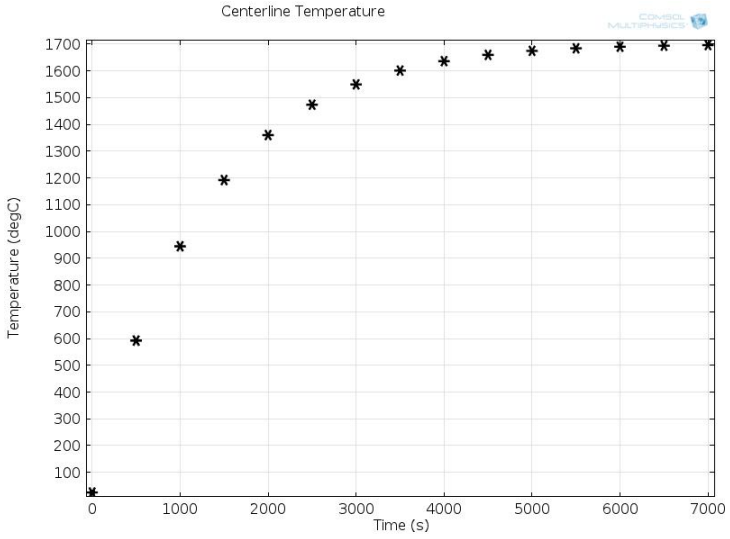

Figure 25 -- Temperature profile along centerline of simulated B_4C packed bed.

as well as an incremental temperature jump expected if a plasma atmosphere addition was made.

The next simulation represented in Figure 25 contained a greater number of spheres in 3D and assumed a graphite cylindrical crucible inside a furnace with a temperature of 1700°C. After

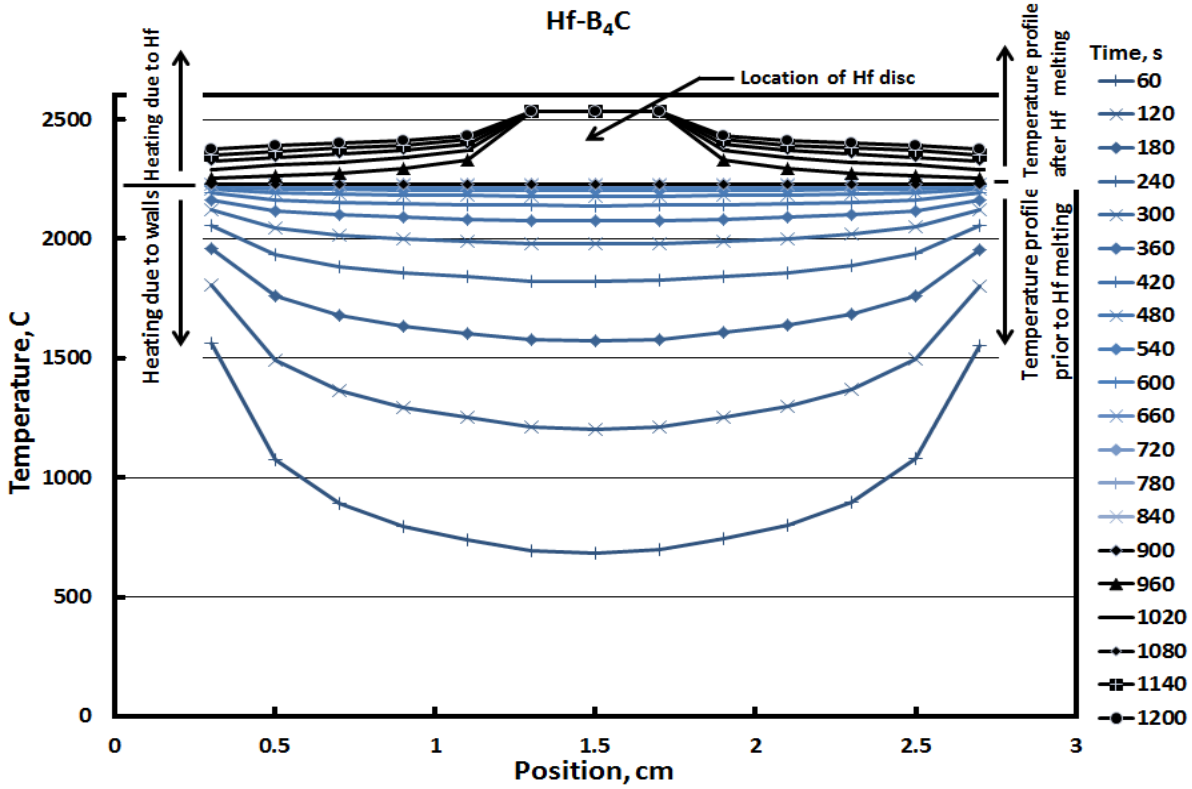

Figure 26 -- Temperature profile acquired from heating a B_4C packed bed with a wall temperature of 2200°C and a Hf disc spiking instantaneously in temperature of 200°C (COMSOL)

an hour and a half (or 500 s), the B_4C particles located at the walls had reached 1700°C though the interior spheres were cooler. Within approximately an hour and a half, the centerline showed that the temperature reached a plateau of 1700°C. These simulations appeared to model the heat transfer better, but the COMSOL software curiously expanded the temperature distribution. The contribution of radiation at temperatures greater than 1000°C were expected to significantly increase, because of the temperature term elevated to the fourth power found in radiative heat transfer. The model replicated a packed bed better than the first simulations but, because the number of spheres was increased, the number of elements also increased which made the computing time increase exponentially.

Using a point evaluation, the temperature distribution was obtained at the centers of all the B_4C spheres in Figures (25) and (26). The plots exhibit the temperature from sphere to sphere in one minute increments. At starting times, a parabolic behavior can be seen since the temperature difference is greater. The temperature profile linearizes as time progresses in approximately 900s.

For the system containing Hf, equilibrium was reached at 2231°C at which the Hf disc melted and reacted exothermically with the B_4C. A temperature increase can be seen from the plot

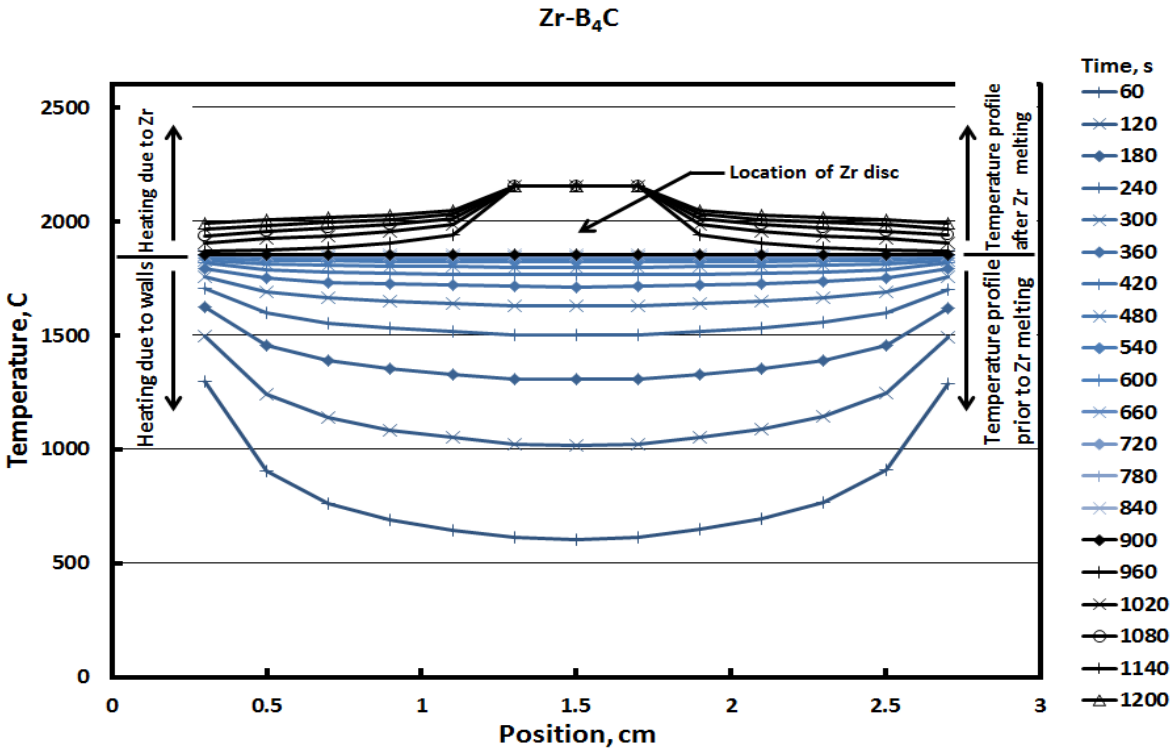

Figure 27 -- Temperature profile acquired from heating a B_4C packed bed with a wall temperature of 1855°C and a Zr disk spiking instantaneously in temperature of 200°C (COMSOL).

in the center where the hafnium was in contact with the boron carbide. The heat then propagated outwards and the rest of the spheres were heated.

The system containing Zr behaved similarly, reaching a plateau at 1855°C before melting the metal and creating the temperature spike in the middle, as shown in Figure 26. In both systems, heating was caused by the crucible walls before reaching temperature plateau since they were at a higher temperature than the rest of the geometry.

After attaining the melting temperature, the metal placed on top of the B_4C melted and reacted releasing heat. At this point, the heating was due to the metal and not the walls, which increased the temperature in the middle. The temperature spike for Zr or Hf caused a sharp temperature gradient within approximately 0.3 cm, which could be significant for surface reactions on carbides. However, the effect of smaller spheres on the heat transfer should be developed further as well as to mimic the actual irregular morphology of the B_4C particles.

For the inclusion of chemical reaction modeling of Ti and O_2 reacting to form TiO_2 was selected and the effects of velocity (Figure 27), pressure (Figure 28), and species concentrations on the reaction were obtained as well as schematic indicating the rate at which TiO_2 forms, as shown again in Figure 27. For future work, ensuring the model was consistent with known Ti oxidation, the surface-plasma interactions could be analyzed to determine whether an oxygen plasma or a CO plasma would cause the surface temperature on the carbide to differ significantly at temperatures greater than 1700 °C . The oxygen may react differently with the carbide if an exothermic reaction occurs. A significant temperature spike on the surface with the presence of a plasma atmosphere is expected. The oxygen and oxygen may react differently with the carbide if an exothermic reaction occurs. A significant temperature spike on the surface with the presence of a plasma atmosphere would certainly aid with densification of carbide particles.

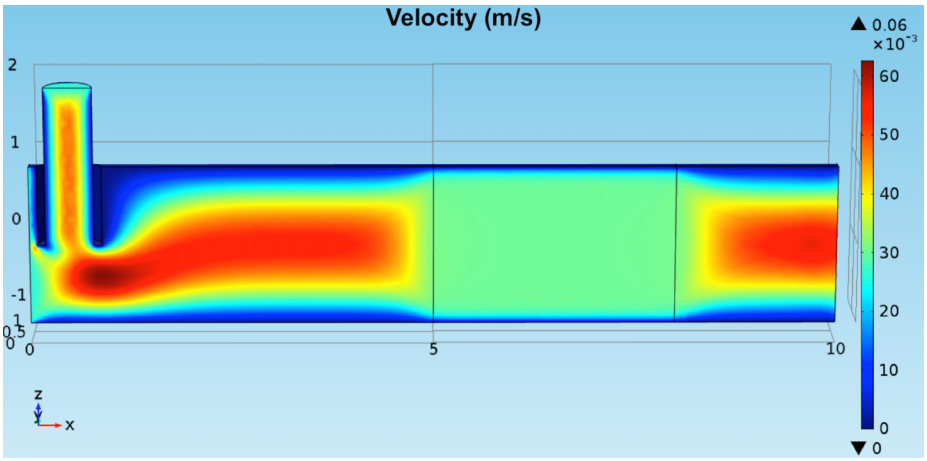

Figure 28 -- The velocity profile determined from the Navier-Stokes equations (COMSOL).

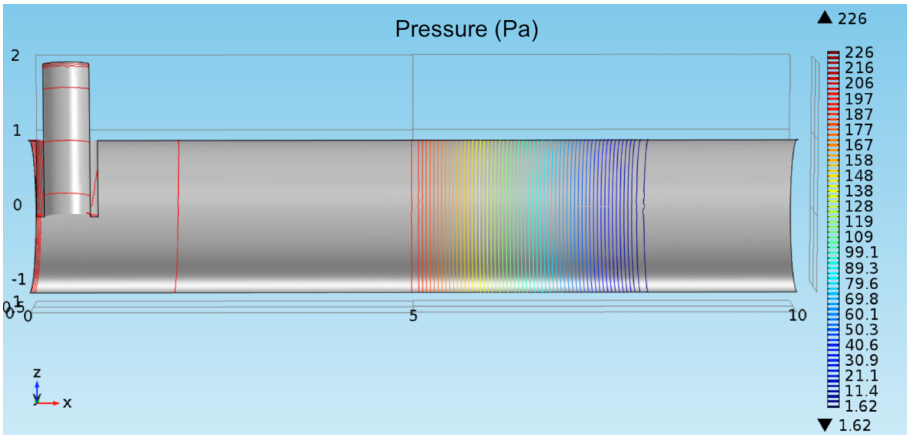

Figure 29 -- The pressure gradients resulting from the Navier-Stokes equations (COMSOL).

4.4 Discussion of Plasma –Surface Reactions with Graphite or Carbides

The next steps for the modeling of plasma-surface reactions would be the effect of temperature and ion bombardment with and without sheathing of the surfaces by using the techniques in the design of fusion devices (e.g., tokamaks) and physical sputtering in thin film devices. Temperature has a significant effect on the chemical sputtering in both areas as Schulter et al. [47]and Pitts et al. [48] have analyzed. For the purposes of the present research, the surface

temperature affects the sputtering of carbon by the flux of incident ions and the material properties. For example, the properties of graphite and the carbide (i.e., B_4C or HfC) depending on the nonstoichiometry could change the yield of chemical erosion. However, the analytical modeling of graphite erosion by hydrogen by Roth and Garcia-Rosales [49] may guide future models even though their analysis was developed for thermonuclear fusion experiments. The thermal plasma expected in a carbide processing would not have the high powered ion flux of a fusion bombardment, but the carbide in a porous media or packed bed must be eroded and then deposited on adjacent surfaces to close pores for densification. The thermal erosion of the carbide by the thermal plasma would include the following terms obtained from Roth and Garcia-Rosales though without the contribution from physical sputtering:

$$Y_{tot} = Y_{therm} + Y_{Surf} \tag{26}$$

The rate of erosion and deposition will depend on the ion flux and the surface temperature with the latter affecting the rate constant of the controlling reaction according to an Arrhenius equation. However, the models developed for hydrogen ions impacting graphite for only erosion reached a saturation or plateau, which occurred curiously about 950 K for the surface temperature with a maximum ion flux of 10^{21} to 10^{24} ions/(m^2s). The ion flux for oxygen and the surface temperature would obviously differ for a HfC, B_4C or TiC surface which would be the objective for future work.

Though the surface reaction of Ti with O_2 to form TiO_2 was partially simulated, the major reaction of adsorbed oxygen with carbide surface may occur with the carbon to form adsorbed CO. Then adsorbed CO (CO_{ad}) will probably leave the surface as CO, as shown in the following reaction sequence:

$$O_2 + 2V = 2O_{ad} \tag{27}$$
$$O_{ad} + C = CO_{ad} \tag{28}$$
$$CO_{ad} = CO \tag{29}$$

The charged species may not enter in the reaction beyond creating more adsorbed oxygen species as suggested above in the formation of adsorbed species depending on the power output, as shown in Figure 8. The power output would be proportional to the ion flux and consequently affect the erosion rate and deposition rate of any carbon onto the adjacent surfaces.

5. Conclusions

The transient surface temperature of particles within a packed bed was simulated to enable ultimately the prediction of plasma-surface reactions at ultra-high temperatures. The motivation for the present study was along two fronts – the plasma processing of materials to spike the surface temperatures and the synthesis of Ti_3AlC in a controlled oxygen potential. The transient temperature simulations determined that a graphite crucible containing B_4C spherical particles

heated from 773 to 1900 K occurred in 840 s though in comparing the temperature profiles of Hf and Zr, they significantly changed more quickly even though the difference in thermal conductivity between B_4C and Hf or Zr was slightly less than an order of magnitude. The transient surface temperature during the oxidation of Ti particles to rutile within a packed bed also spiked the temperature of the bed indicating that the processing temperature may cause a significant temperature gradient along the cross-section of the bed depending on its content of reactive metals.

The Ti_3AlC was synthesized with a mixture of 39Ti-14Al-47TiC (in wt%) heated to 1973 K by using a pseudo-isopiestic technique to control the oxygen potential. After reacting the mixture, a three-phase field of Ti_3AlC-Ti_2AlC-TiC was acquired and subsequently oxidized at 1873 K. The carbide formed a duplex scale with the inner layer consisting of TiO, Al_2O_3 and Al_4CO_4 with an outer layer composed of TiO_2, Al_2O_3 and Al_2TiO_5. From the effective diffusion coefficient obtained from the measured scale thickness assuming Wagner's parabolic growth rate, the analysis suggests that Ti ions migrate outwardly as the oxygen ions diffuse inwardly during scale growth.

The oxygen potential affects the plasma-surface reactions, as expected, though the adsorption and desorption of oxygen becomes more difficult to assess with decreasing oxygen atmospheres. The error in the predictability the desorption with decreasing oxygen partial pressures less than 10^{-6} atm may become problematic, because plasma-surface reactions may occur at oxygen potentials less than 10^{-20} atm when processing elements from the Ti or rare earth metal family. The power used to generate the plasma atmosphere influences the adsorption and desorption of oxygen occurring on surfaces. The adsorption and desorption of the oxygen depends on a rate-determining step involving surface sites within a plasma atmosphere as similarly obtained for oxygen interacting with surfaces without a plasma atmosphere.

6. Personnel Supported

Alejandro Garcia and Alberto Delgado were fully supported through their master's degree and baccalaureate degree, respectively, both in mechanical engineering. Sanjay Shantha-Kumar and Arturo Medina were partially supported toward their doctoral and master's degrees, respectively, with Sanjay aiding Alberto in his experimental design and microstructural analysis and Arturo exchanging computational techniques with Alejandro. Samia Afin who graduated with a doctoral degree in environmental science/engineering degree also contributed in managing the computational hardware and software toward the end of the project.

7. References

1. M. I. Boulos, P. Fauchais, and E. Pfender, *Thermal Plasmas* (Springer US, Boston, MA, 1994).

2. K. Natesan and W. T. Bakker, J. Mater. Energy Syst. **6**, 163 (1984).

3. P. Kofstad, in (Elsevier Applied Science, 1988), pp. 316–319,389–390.

4. G. H. Meier, in *Oxid. High Temp. Intermet.*, edited by J. Grobstein, T. and Doychak (The Minerals, Metals and Materials Society, Warrendale, PA, 1988), pp. 1–16.

5. H. C. Graham and H. H. Davis, J. Am. Ceram. Soc. **54**, 89 (1971).

6. D. R. Sigler, Oxid. Met. **32**, 337 (1989).

7. G. C. W. and F. H. Stott, in *High Temp. Corros.*, edited by R. A. Rapp (National Association of Corrosion Engineers, 1983), pp. 227–250.

8. K. Natesan and W. T. Bakker, *Corrosion and Mechanical Behaviour of Materials for Coal Gasification Applications* (1980).

9. H. E. Frankel and S. J. Dapkunas, Thin Solid Films **45**, 211 (1977).

10. R. A. Rapp, J. H. Devan, D. L. Douglass, P. C. Nordine, F. S. Pettit, and D. P. Whittle, in *Mater. Sci. Eng.* (1981), pp. 1–17.

11. M. P. Brady, P. F. Tortorelli, K. L. More, and L. R. Walker, Oxid. Met. **74**, 1 (2010).

12. C. W. Bale, E. Belisle, P. Chartrand, S. A. Decterov, G. Eriksson, K. Hack, I. H. Jung, Y. B. Kang, J. Melancon, A. D. Pelton, C. Robelin, and S. Petersen, Calphad Comput. Coupling Phase Diagrams Thermochem. **33**, 295 (2009).

13. P. Waldner and G. Eriksson, Calphad Comput. Coupling Phase Diagrams Thermochem. **23**, 189 (1999).

14. H. Nyman, T. Talonen, A. Roine, M. Hupa, and J. Corander, Metall. Mater. Trans. B **43**, 1113 (2012).

15. F. A. Golightly, F. H. Stott, and G. C. Wood, Oxid. Met. **10**, 163 (1976).

16. H. Hindam and D. P. Whittle, Oxid. Met. **18**, 245 (1982).

17. P. F. Natesan, K.; Tortorelli, **A258**, 115 (1998).

18. R. J. Christensen, V. K. Tolpygo, and D. R. Clarke, Acta Mater. **45**, 1761 (1997).

19. T. Ramanarayanan, M. Raghavan, and R. Petkovic-Luton, J. Electrochem. Soc. **131**, 923 (1984).

20. D. Schiferl, A. I. Katz, R. L. Mills, L. C. Schmidt, E. F. Skelton, W. T. Elam, A. W. Webb, and M. Schaefer, 897 (1986).

21. K. Przybylski, A. J. Garratt-Reed, B. A. Pint, E. P. Katz, and G. J. Yurek, J. Electrochem. Soc. **134**, 3207 (1987).

22. B. . Pint, I. . Wright, W. . Lee, Y. Zhang, K. Prüßner, and K. . Alexander, Mater. Sci. Eng. A **245**, 201 (1998).

23. P. Y. Hou and G. D. Ackerman, Appl. Surf. Sci. **178**, 156 (2001).

24. P. Y. Hou, X. F. Zhang, and R. M. Cannon, Scr. Mater. **50**, 45 (2004).

25. P. Y. Hou, J. Am. Ceram. Soc. **86**, 660 (2003).

26. G. Vasquez and A. Bronson, Metall. Mater. Trans. A Phys. Metall. Mater. Sci. **36**, (2005).

27. M. P. Brady and P. F. Tortorelli, Intermet. Adv. Met. Mater. - A Symp. Dedic. to Dr. C.T. Liu, 3-6 March 2003, San Diego, CA, USA **12**, 779 (2004).

28. A. Lashtabeg, J. Canales-Vazquez, J. T. S. Irvine, and J. L. Bradley, Chem. Mater. **21**, 3549 (2009).

29. R. A. Pasternak and B. Evans, J. Electrochem. Soc. **114** , 452 (1967).

30. P. Kofstad, *High Temperature Corrosion* (Elsevier Applied Science, New York, 1988).

31. H. G. Park, A. Gokhale, P. Kumar, and R. Abbaschian, High Temp. Mater. Process. **11**, (1993).

32. V. S. Stubican, in *Adv. Ceram. Vol. 24 Sci. Technol. Zirconia III* (American Ceramic Society, Inc., 1988), pp. 71–83.

33. A. Fridman, *Plasma Chemistry* (Cambridge University Press, 2008).

34. A. Fridman and L. A. Kennedy, *Plasma Physics and Engineering* (CRC press, 2004).

35. V. M. Donnelly, J. Guha, and L. Stafford, J. Vac. Sci. Technol. A Vacuum, Surfaces, Film. **29**, 010801 (2011).

36. B. A. Helmer, *Computer Simulations of Plasma-Surface Chemistry* (n.d.).

37. G. P. Kota, J. W. Coburn, and D. B. Graves, J. Vac. Sci. Technol. A **16**, (1998).

38. C. Lee, J. Electrochem. Soc. **141**, 1546 (1994).

39. P. F. Kurunczi, J. Guha, and V. M. Donnelly, Phys. Rev. Lett. **96**, 1 (2006).

40. P. W. Wang, J. Woo, M. Avila, J. Garcia, A. Bronson, and S. K. Varma, J. Mater. Sci. **38**, 489 (2003).

41. H J Grabke and and G Horz, Annu. Rev. Mater. Sci. **7**, 155 (1977).

42. P. F. Kurunczi, J. Guha, and and V. M. Donnelly, J. Phys. Chem. B **109**, 20989 (2005).

43. J. Guha, P. Kurunczi, L. Stafford, V. M. Donnelly, and Y. K. Pu, J. Phys. Chem. C **112**, 8963 (2008).

44. D. Bandyopadhyay, R. C. Sharma, and N. Chakraborti, J. Phase Equilibria **21**, 195 (2000).

45. A. Muan and E. F. Osborn, *Phase Equilibria among Oxides in Steelmaking* (Addison-Wesley Publishing Company, Inc., 1965).

46. Comsol, Introduction to Heat Transfer Module, pp. 1-34 (2012).

47. M. Schlüter, C. Hopf, T. Schwarz-Selinger, and W. Jacob, J. Nucl. Mater. **376**, 33 (2008).

48. R. A. Pitts, S. Carpentier, F. Escourbiac, T. Hirai, V. Komarov, S. Lisgo, A. S. Kukushkin, A. Loarte, M. Merola, A. Sashala Naik, R. Mitteau, M. Sugihara, B. Bazylev, and P. C. Stangeby, J. Nucl. Mater. **438**, 48 (2013).

49. J. Roth and C. Garcia-Rosales, Nucl. Fusion **37**, 897 (2002).